13

A Two-Dimensional Perspective on CH_4 Isotope Clumping

Distinguishing Process from Source

EDWARD D. YOUNG

13.1 Introduction

Isotope ratios have been used extensively to trace the origins of methane gases (e.g. Schoell 1980). For this purpose, the stable isotope ratios $^{13}C/^{12}C$ and D/H have been paramount. These ratios refer to the atomic abundances of the rare isotopes of carbon and hydrogen relative to the more abundant isotopes, in aggregate, and inclusive of all of the methane isotopic molecular species in a sample of gas. We therefore refer to these ratios as "bulk" isotope ratios. The term "isotopologue" refers to specific isotopic versions of the *molecules*. For example, the "$^{12}CH_3D$ isotopologue" refers to the $^{12}CH_3D$ + $^{12}CH_2DH$ + $^{12}CHDH_2$ + $^{12}CDH_3$ permutations of the D-substituted isotopic species of CH_4 collectively. In the geosciences, the term "clumping" denotes more than one heavy isotope in a single molecule or molecular unit (e.g. $^{13}C^{18}O^{16}O^{16}O$ + $^{13}C^{16}O^{18}O^{16}O$ + $^{13}C^{16}O^{16}O^{18}O$ in the CO_3^{2-} moiety within the $CaCO_3$ crystalline structure). In this chapter, the results of recent studies of the relative abundances of the clumped methane species $^{13}CH_3D$ and $^{12}CH_2D_2$ measured at the University of California, Los Angeles (UCLA) are summarized.

We begin with a description of the goals of this research program. The original excitement about making use of the $^{13}C-^{18}O$ multiply substituted isotopologue of CO_2, $^{13}C^{18}O^{16}O$ + $^{13}C^{16}O^{18}O$, derived from acid digestion of carbonate was due to the prospect of removing the various logical degeneracies that have historically plagued our interpretations of the significance of $^{18}O/^{16}O$ (usually expressed as $\delta^{18}O$ values, the per mil differences in $^{18}O/^{16}O$ from a standard material) in carbonates (Eiler et al. 2005). Marine carbonate oxygen isotope ratios can vary in response to temperature, ice volume, or secular variations in the $\delta^{18}O$ of the oceans. By using the temperature-dependent propensity of ^{13}C and ^{18}O to form bonds as a homogeneous (as in a single-phase as opposed to heterogeneous fractionation between two separate phases, in this case carbonate and water) thermometer, the relationship between bulk $\delta^{18}O$ in the carbonate and that in the water becomes irrelevant if the goal is to deduce temperature of formation. The goal, therefore, was to develop an isotopic tracer in which the bulk isotope ratios are normalized out.

The CH_4 clumping project at UCLA, in collaboration with the Carnegie Institution of Science, began in 2008 with the prospects for funding by the Deep Carbon Observatory and an eye toward replicating the powerful aspects of carbonate clumping for methane.

388

Figure 13.1 Mass spectrometer used to separate the two rare mass-18 isotopologues of CH$_4$ gas molecules. The instrument – the Panorama – is housed at UCLA and is the first of its kind (Young et al. 2016).

In particular, the group originally sought to distinguish biotic from abiotic methane based largely on temperature of formation, but also based on reaction pathways. Even before delivery of our unique mass spectrometer built for this purpose (Figure 13.1), methane experts (in particular Barbara Sherwood Lollar, University of Toronto) warned of the naivety of assuming that methane molecules would have simple, single-stage histories, and emphasized in particular the important role of mixing, the breadth of abiotic organic reactions over the range of temperatures that might be involved, and the complexity of microbial methanogenesis pathways and associated kinetic fractionation effects. In response, we developed predictions for these various phenomena in preparation for the new data to come.

The work described herein is the realization of those original goals to use two mass-18 isotopologues of CH$_4$ to disambiguate the multiple possible sources of methane gases using a process-oriented approach. Just as carbonate isotope clumping can break the degeneracy between seawater δ^{18}O and temperature of formation, the use of two methane mass-18 isotopologues should remove the ambiguities arising from variations in the ^{13}C/^{12}C and D/H ratios of the carbon and hydrogen sources of methane. We seek to eliminate, or at least mitigate, the uncertainties surrounding the use of δ^{13}C and δD as the primary arbiters for the origin of methane gas. Even when combined with other important tracers of gas provenance like C$_1$/C$_2$+ (the ratio of CH$_4$ to C$_2$H$_6$ + C$_3$H$_8$, etc.), ambiguities regarding the provenance of methane often remain when relying on bulk isotope ratios. Rules of thumb have been constructed based on years of observations. One example is that a decrease in ^{13}C/^{12}C (δ^{13}C) with increasing carbon number for the alkanes can be evidence for abiotic formation. But these rules are, for the most part, empiricisms and fraught with exceptions. The goal of the studies described here is to make use of the relative concentrations of ^{13}CH$_3$D and ^{12}CH$_2$D$_2$ together in methane gas to remove the uncertainties plaguing other tracers while avoiding adding just another layer of complexity.

This means using what these isotopologues are telling us in order to gain a fresh vantage point for our views on the origin of methane and to find out if we might be led astray by some of the earlier criteria for provenance.

Perhaps the most succinct way to summarize this perspective is that the isotopic bond ordering, or clumping, traces process, while bulk isotope ratios trace both process and source isotopic compositions. By following the isotopic bond ordering, we are isolating process from variations in source material.

13.2 Temperature

The concept of using "clumping" of heavy isotopes in a molecule as a thermometer is understood by referencing the null condition of the purely stochastic distribution of isotopes among the molecules of interest. In the case of methane, one is concerned with the fraction of carbon that is composed of the heavy isotope, $X(^{13}C) = {}^{13}C/({}^{13}C + {}^{12}C)$, and the fraction of the hydrogen isotopes that is composed of deuterium, $X(D) = D/(D + H)$. In the case of purely random distributions of isotopes among molecules, the products of fractional isotope abundances yield the joint probabilities, or predicted concentrations, for the isotopologues. For example, $X(^{12}CH_3D) = X(^{12}C)(X(H))^3 X(D)$, where the exponent accounts for the simultaneous occurrence of H at three positions. Isotopologue abundances are not generally random, however. The temperature-dependent exchange of isotopes between isotopologues occurs by reactions such as

$$^{13}CH_4 + {}^{12}CH_3D \rightleftarrows {}^{12}CH_4 + {}^{13}CH_3D. \tag{13.1}$$
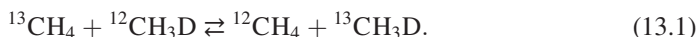
The equilibrium constant for this reaction is

$$k_{Eq, {}^{13}CD} = \frac{[^{13}CH_3D][^{12}CH_4]}{[^{13}CH_4][^{12}CH_3D]}, \tag{13.2}$$

where the square brackets denote concentrations that can be equated with the fractional abundances of the isotopologues by number. At high temperatures (≥ 1000 K), the distributions of isotopologues are effectively random (stochastic) and substitution of the fractional abundances into the equilibrium constant in (13.2) yields (e.g. Richet et al. 1977):

$$k_{Eq, {}^{13}CD} = \frac{[^{13}CH_3D][^{12}CH_4]}{[^{13}CH_4][^{12}CH_3D]} = \frac{4X(^{13}C)\ (X(H))^3 X(D)\ X(^{12}C)\ (X(H))^4}{4X(^{12}C)\ (X(H))^3 X(D)\ X(^{13}C)\ (X(H))^4} = 1. \tag{13.3}$$

Equation (13.3) shows that an equilibrium constant of unity in this case corresponds to a purely random distribution of isotopes among the molecules. At lower temperatures, the stabilizing effects of two heavy isotopes bonded together take hold and the equilibrium constant in (13.2) gets progressively larger as temperature decreases. This enhancement in rare multiply substituted isotopologues, or clumping, can be expressed in delta notation and in per mil units as

$$\Delta_{^{13}CH_3D} = 10^3 \left(\frac{X(^{13}CH_3D)}{X(^{13}CH_3D)_{Stochastic}} - 1 \right). \tag{13.4}$$

Similarly, internal isotope exchange leading to doubly deuterated methane can be described by the reaction

$$2\,^{12}CH_3D \rightleftarrows\, ^{12}CH_2D_2 + \,^{12}CH_4, \tag{13.5}$$

with the equilibrium constant

$$k_{Eq,\,CH_2D_2} = \frac{[^{12}CH_2D_2]\,[^{12}CH_4]}{[^{12}CH_3D]^2}. \tag{13.6}$$

The stochastic value for the equilibrium constant for reaction (13.6) is

$$k_{Eq,\,^{12}CH_2D_2} = \frac{[^{12}CH_2D_2]\,[^{12}CH_4]}{[^{12}CH_3D]^2} = \frac{6X(^{12}C)\,(X(H))^2 X(D)^2\ X(^{12}C)\,(X(H))^4}{\left[4X(^{12}C)(X(H))^3 X(D)\right]^2} = \frac{3}{8},$$
$$\tag{13.7}$$

such that a stochastic distribution of isotopes leads to an equilibrium constant of 3/8. Per mil departures from this stochastic ratio are quantified using

$$\Delta_{^{12}CH_2D_2} = 10^3 \left(\frac{X(^{12}CH_2D_2)}{X(^{12}CH_2D_2)_{Stochastic}} - 1 \right). \tag{13.8}$$

The two parameters $\Delta^{12}CH_2D_2$ and $\Delta^{13}CH_3D$ are independent intramolecular thermometers where thermodynamic equilibrium applies. The relationships between temperature and both $\Delta^{12}CH_2D_2$ and $\Delta^{13}CH_3D$ are calculable (e.g. Ma et al. 2008; Webb and Miller 2014; Liu and Liu 2016) and loci of thermodynamic equilibrium in plots of $\Delta^{12}CH_2D_2$ versus $\Delta^{13}CH_3D$ serve as useful references in the plots to follow (Figure 13.2).

13.3 Criteria for Intra-CH₄ Thermodynamic Equilibrium

Criteria for establishing whether or not methane molecules are in isotopologue equilibrium with one another is a first-order requisite for making use of these new data. A datum for a sample of methane gas that plots on the curve in Figure 13.2 would be regarded as representing thermodynamic equilibrium at the indicated temperature by virtue of the concordant temperatures recorded by both clumped species. However, in the absence of data for both $\Delta^{13}CH_3D$ and $\Delta^{12}CH_2D_2$, Figure 13.2 cannot be used to establish equilibrium or nonequilibrium.

While the large-geometry mass spectrometer that permits use of Figure 13.2 was being built for UCLA, two other groups published several papers based on application of the single mass-18 isotopologue $^{13}CH_3D$, or unresolved $^{13}CH_3D$ and $^{12}CH_2D_2$, where the two

Edward D. Young

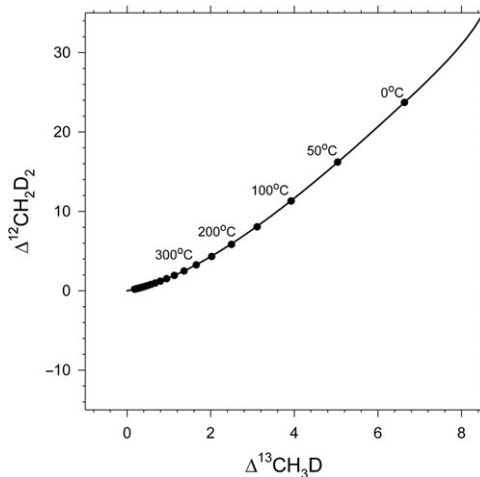Figure 13.2 Plot of thermodynamic equilibrium among methane isotopologues as a function of temperature in $\Delta^{12}CH_2D_2$ versus $\Delta^{13}CH_3D$ space (after Young et al. 2017).

species are lumped together in one measurement (Stolper et al. 2014, 2015; Wang et al. 2016). Their conclusions were reviewed by Douglas et al. (2017), who describe the "reversibility of methanogensis" hypothesis that was used in several of these papers to explain why temperatures derived using the relative abundances of $^{13}CH_3D$ are not always reasonable (Wang et al. 2015). However, our studies of $\Delta^{13}CH_3D$ and $\Delta^{12}CH_2D_2$ suggest that the rate of methanogenesis is not the primary factor that controls isotope clumping in microbialgenic methane.

The reversibility of the methanogenesis concept is based on earlier work relating D/H and $^{13}C/^{12}C$ in microbial methanogenesis to the chemical potential gradient between reactants H_2, CO_2, or methyl groups and the product CH_4 (Valentine et al. 2004; Penning et al. 2005). This hypothesis posits that the degree of isotopic equilibrium among CH_4 molecules will depend on the rate of methanogenesis (see below). In these studies, the primary tool for establishing whether or not $\Delta^{13}CH_3D$ (or the similar parameter Δ_{18}, which is used where the two mass-18 species are unresolved, since normally $^{13}CH_3D \gg {}^{12}CH_2D_2$ in abundance) represents equilibrium is whether or not the observed D/H partitioning between water and methane, $\alpha_{D/H}$ (H_2O–CH_4) (the fractionation factor $\alpha_{D/H}$ between water and methane is defined as D/H of water divided by D/H of methane), is consistent with the temperature deduced from the single mass-18 clumping temperature. In this scenario, if $\Delta^{13}CH_3D$ is out of equilibrium but progresses toward equilibrium, there will be a correlation between the $\Delta^{13}CH_3D$ (Δ_{18}) and δD of the methane (unless, by coincidence, the methane is already in equilibrium with water). Of course, the obvious disadvantage of this approach as the primary criterion for intra-methane equilibrium is that one has to have the δD of water coexisting with the methane of interest, and there are circumstances where water samples are either impractical to obtain or nonexistent.
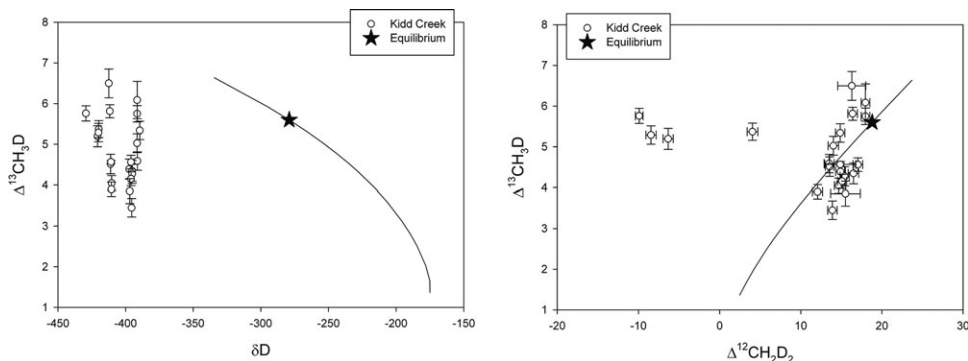
Figure 13.3 Kidd Creek Mine CH_4 data showing the $\Delta^{13}CH_3D$ versus two different potential measures of the degree of intra-CH_4 isotopic equilibrium, δD, and $\Delta^{12}CH_2D_2$. Curves show equilibrium (at fixed δD water = $-32\permil$) from 0ºC to 350ºC. The stars represent equilibrium at 30ºC. The data show a time evolution toward equilibrium in $\Delta^{12}CH_2D_2$ (Young et al. 2017).

In addition to being inconvenient, the water δD criterion for methane isotopologue equilibrium is not universal, as illustrated using $\Delta^{13}CH_3D$ and $\Delta^{12}CH_2D_2$ data from the Kidd Creek Mine, Timmins, Ontario, Canada (Young et al. 2017). Figure 13.3 shows $\Delta^{13}CH_3D$ versus δD and versus $\Delta^{12}CH_2D_2$ for CH_4 from Kidd Creek. Because the δD values of the waters in the mine are generally within a few per mil of $-30\permil$ standard mean ocean water (SMOW), the δD of CH_4 is a measure of $\alpha_{D/H}$ (H_2O–CH_4). One sees that while $\Delta^{12}CH_2D_2$ shows a clear progression toward equilibrium, δD does not. At this location, δD is not especially useful as an indicator of equilibrium, but $\Delta^{12}CH_2D_2$ is. This confirms that heterogeneous (water versus gaseous CH_4) disequilibrium in D/H can persist even as homogeneous equilibrium (exchange among gaseous CH_4 molecules) is approached.

13.4 Kinetics

An understanding of the effects of kinetics on methane isotope clumping is also crucial for interpreting these new data. The idea that the *rate* of methanogensis controls the degree of departure from thermodynamic equilibrium among methane isotopologues has been put forward several times in the literature, perhaps in most complete form in the supplement to Wang et al. (2015) in which the authors invoke "Michaelis–Menten" kinetics for the H addition steps to build methane. This kinetic formalism is commonly used in the biochemistry of enzymes. The equations represent simple transition state-like kinetics where the transition state is replaced by the enzyme–substrate complex:

$$E + S \underset{k_r}{\overset{k_f}{\rightleftarrows}} ES \xrightarrow{k_{cat}} E + P, \tag{13.9}$$
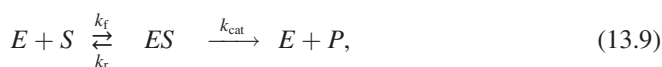
where E is the enzyme, S is the substrate, ES is the substrate bound to the catalyzing enzyme (the enzyme–substrate complex), and P is the product. The forward and reverse

rate constants for binding are shown in (13.9), and the subscript "cat" signifies the catalyzed rate constant. The binding of the substrate to the enzyme by a reversible (equilibrium) process is the foundation of Michaelis–Menten kinetics, just as it is foundational for transition state theory. For this equilibrium, the forward and reverse rates are by definition equal:

$$k_f[E][S] = k_r[ES]. \tag{13.10}$$

Mass balance requires $[E] = [E]_0 - [ES]$, where the "0" subscript signifies the initial concentration. After some manipulation, (13.10) leads to the simple first-order rate equation for product P:

$$\frac{d[P]}{dt} = k_{cat} \frac{[E]_o[S]}{\left(\dfrac{k_r}{k_f}\right) + [S]}. \tag{13.11}$$

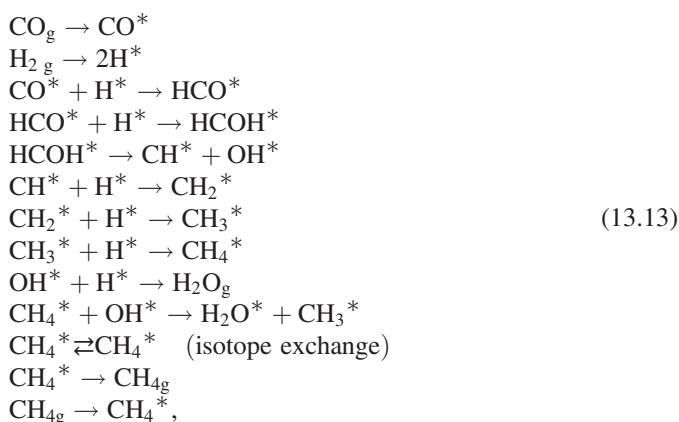Comparing the above to the often-cited Michaelis–Menten equation for an enzyme-catalyzed reaction:

$$\frac{d[P]}{dt} = \frac{V_{max}[S]}{k_m + [S]}, \tag{13.12}$$

where k_m is the "affinity" for the enzyme plus substrate, one sees by inspection that (13.11) is equivalent to (13.12), where the "affinity" for the bound substrate is here equivalent to k_r/k_f and the maximum rate used in the Michaelis–Menten formulation, V_{max}, is $k_{cat}[E]_0$. Notice that when the substrate is plentiful such that $[S] \gg k_r/k_f$, the rate of product production is maximized since $d[P]/dt \approx V_m = k_{cat}[E]_0$. Conversely, where the concentration of the substrate is very small, leading to starvation and thus $[S] \ll k_r/k_f$, we have $d[P]/dt \approx k_{cat}[E]_0[S]/(k_r/k_f)$, which is the maximum rate multiplied by $[S]k_f/k_r$, and so smaller than the maximum rate of reaction. What is more, in this case, both the forward and reverse reactions to form the *ES* complex are involved, leading to the suggestion that reversibility, or equilibrium, controls the attachment of the substrate to the enzyme.

While (13.11) and (13.12) are handy for describing how the rate of product formation depends on three postulated rate constants, they offer little or no fundamental insights into the effects on isotope clumping. For example, we do not know *a priori* which reaction in the sequence of steps leading to CH_4 formation is properly described by (13.9). Importantly, the kinetic isotope effects (KIEs) and/or equilibrium isotope effects (EIEs) for each of the steps in (13.9) can be adjusted to fit the data, but this relegates (13.11) and (13.12) to little more than a framework for applying fit parameters. Measurements of both $\Delta^{13}CH_3D$ and $\Delta^{12}CH_2D_2$ suggest that the "reversibility of methanogenesis" hypothesis is not the best explanation for the clumping of isotopes into methane of microbial origin.

Here, we consider an alternative approach to explaining the effects of microbial methanogenesis on methane mass-18 isotopologue abundances based on the large degree of disequilibrium exhibited by the low $\Delta^{12}CH_2D_2$ values characteristic of microbialgenic gas in combination with highly variable $\Delta^{13}CH_3D$ values. For this purpose, we take the

reaction scheme used by Young et al. (2017) as an analogue for hydrogenotrophic methanogenesis and the steps leading to the net reaction $CO_2 + 4H_2 \rightarrow CH_4 + 2H_2O$. Young et al. (2017) used the reaction scheme for the Fischer–Tropsch synthesis of methane on a cobalt (Co) catalyst suggested by Qi et al. (2014). Methanation of CO_2 can occur by conversion first to CO, with the subsequent steps being the same as those for direct methanation of CO (Wang et al. 2011). The kinetic model presented here is therefore relevant to methane production from CO_2 as well. We added isotope exchange between methane molecules on the surface, desorption and adsorption of CH_4 gas, and attack of CH_4 by OH to the elementary steps leading to methane formation. The set of reactions can be represented by these basic reactions and their isotopically substituted equivalents:

$$
\begin{aligned}
&CO_g \rightarrow CO^* \\
&H_{2\,g} \rightarrow 2H^* \\
&CO^* + H^* \rightarrow HCO^* \\
&HCO^* + H^* \rightarrow HCOH^* \\
&HCOH^* \rightarrow CH^* + OH^* \\
&CH^* + H^* \rightarrow CH_2{}^* \\
&CH_2{}^* + H^* \rightarrow CH_3{}^* \\
&CH_3{}^* + H^* \rightarrow CH_4{}^* \\
&OH^* + H^* \rightarrow H_2O_g \\
&CH_4{}^* + OH^* \rightarrow H_2O^* + CH_3{}^* \\
&CH_4{}^* \rightleftarrows CH_4{}^* \quad \text{(isotope exchange)} \\
&CH_4{}^* \rightarrow CH_{4g} \\
&CH_{4g} \rightarrow CH_4{}^*,
\end{aligned}
\tag{13.13}
$$

where an asterisk signifies a surface-adsorbed species and a subscript "g" refers to a gas species. With all isotopologues and isotopomers, the model consists of 124 species and 796 reactions. The rate constants for the reactions are of the form

$$
k_f = Q_{\text{Tun}} \frac{k_b T}{h} \frac{q^+}{\prod_r q_r} \left(\frac{-Ea}{k_b T} \right),
\tag{13.14}
$$

where k_b is the Boltzmann constant, h is the Planck constant, Ea is the activation energy, q_r are the partition functions for reactant species r, q^+ is the partition function for the transition state, and Q_{Tun} is a correction for quantum tunneling. The 124 ordinary differential equations comprising the model are solved numerically using the Lawrence Livermore ordinary differential equation solver (*DLSODE*). Activation energies for the methane formation reactions were taken from Qi et al. (2014). Values for *Ea* for the reaction $CH_4 + OH$ were taken from Haghnegahdar et al. (2015). The tunneling correction is from Bell (1959, 1980).
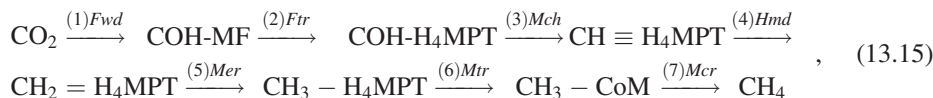
Young et al. (2017) used forward rate constants throughout the reaction network to characterize the effects of the kinetics alone on product methane isotopologues. We concluded in that work that the very negative $\Delta^{12}CH_2D_2$ values were due either to the influence of quantum tunneling or to the combinatorial effect of accessing multiple sources of hydrogen produced by very different fractionation factors involving D/H during the

assembly of methane. We favored tunneling in particular for our measurements of products from the Sabatier reaction in the laboratory ($CO_2 + 4H_2 \rightarrow CH_4 + 2H_2O$) mainly because invoking a slight difference in tunneling for $^{13}C–H$ bonds versus $^{12}C–H$ bonds could account for the combination of very positive $\Delta^{13}CH_3D$ values along with the negative $\Delta^{12}CH_2D_2$ values (note: an error in that paper has the ratio of tunneling length scales a_D/a_H = 1.005, when in fact it is the ratio of $a_{13C–H,D}/a_{12C–H,D}$ that was fit to 1.005 to explain the high $\Delta^{13}CH_3D$ values in the Sabatier reaction; see below). We noted that a combinatorial effect (e.g. Yeung et al. 2015; Rockmann et al. 2016; Yeung 2016) may be important for microbial methanogenesis, but we also expressed concern that the required differences in D/H between pools of hydrogen would need to be very large.

However, Cao et al. (2019) have argued recently that adding certain equilibrium steps into our reaction network can indeed produce the requisite large differences in D/H among pools of hydrogen that can reproduce the very low $\Delta^{12}CH_2D_2$ values observed in microbialgenic methane gases. Here, we take their suggestion and investigate the effects of reversibility on the clumping in the reaction network. For these calculations, the KIE and EIE fractionation factors for each reaction step provided by Qi et al. (2014) are used.
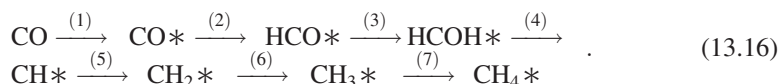
Why would a metal-catalyzed reaction scheme have anything to do with the microbial production of CH_4? What advantage is there in trying to use this reaction scheme to address the microbialgenesis of methane? The basic conceit is that the metal surface simulates the enzymes that afford catalyzed transfer of electrons and protons back and forth during the reaction scheme, and that it is the nature of the various C_1 C–H moieties and their bond stiffness that actually control the isotope effects, regardless of the molecule to which they are bound. This may be useful insofar as at least we are using well-characterized KIE and EIE fractionation factors rather than making them up to explain the data. The logic is that despite the potential failings of the analogy, there is benefit in using a real physicochemical model to try to explain what we are seeing. This model is used in lieu of a detailed understanding of the isotope effects attending each step of the enzymatically catalyzed reactions.

With this in mind, one can observe that the steps of building CH_4 molecules from $CO_2 + H_2$ by enzymes and from $CO + H_2$ on metals are broadly similar. The reaction pathway for hydrogenotrophic addition of hydrogen to form methane as given by Lieber et al. (2014) for *Methanococcus maripaludis* is

$$
\begin{aligned}
&CO_2 \xrightarrow{(1)Fwd} COH\text{-}MF \xrightarrow{(2)Ftr} COH\text{-}H_4MPT \xrightarrow{(3)Mch} CH \equiv H_4MPT \xrightarrow{(4)Hmd} \\
&CH_2 = H_4MPT \xrightarrow{(5)Mer} CH_3 - H_4MPT \xrightarrow{(6)Mtr} CH_3 - CoM \xrightarrow{(7)Mcr} CH_4
\end{aligned}
\quad, \quad (13.15)
$$

where the facilitating enzymes are shown above the arrows (e.g. *Ftr* = formyltransferase; numbers are for reference only) and the C_1 carriers are shown as the molecule acronyms (e.g. H_4MPT = tetrahydromethanopterin). As described by Shima et al. (2002), these steps comprise a series of C_1 molecules that act as terminal electron acceptors (oxidants that themselves are reduced) where carbon is progressively reduced, with each transfer of C_1 facilitated by the indicated enzyme. For example, COH is transferred from the methanofuran molecule to the next C_1 carrier H_4MPT by the enzyme *Ftr*. The subsequent

conveyance of COH to CH (step (3)) is facilitated by methenyl-H$_4$MPT cyclohydrolase (*Mch*). The last step in which the CH$_3$ in methyl-coenzyme M (CH$_3$–CoM) is reduced to methane is facilitated by the methyl-coenzyme M reductase (*Mcr*); *Mcr* is the focus of a lot of attention because it is common to methanogens and anaerobic methanotrophs and is involved in that last step that is common to both. Now compare this with the reaction network in (13.13) written in similar fashion:

$$\begin{aligned}&\text{CO} \xrightarrow{(1)} \text{CO}* \xrightarrow{(2)} \text{HCO}* \xrightarrow{(3)} \text{HCOH}* \xrightarrow{(4)}\\ &\text{CH}* \xrightarrow{(5)} \text{CH}_2* \xrightarrow{(6)} \text{CH}_3* \xrightarrow{(7)} \text{CH}_4*\end{aligned} \quad . \tag{13.16}$$

The reactions in (13.15) and in (13.16) both utilize H$_2$ as the main source of electrons for reduction. In both reaction sequences, C$_1$ passes from oxidized carbon through an alcohol/formyl molecule to a formaldehyde-like molecule followed by progressive reduction by proton addition.

The effects of kinetics versus equilibrium for each of the steps that produce methane are investigated by using the reactions in (13.16) as analogues for the reactions in (13.15) and examining the consequences of imposing various combinations of equilibrium versus kinetics for each step. Borrowing terminology suggested by Cao and Bao, we can refer to this using the vector [0, 0, 0, 0, 0, 0, 0] to signify where all seven steps are kinetic, or [1, 1, 1, 1, 1, 1, 1] to indicate where all seven steps are completely reversible. Intermediate circumstances are represented accordingly; for example, where the first three steps are equilibrium, we have [1, 1, 1, 0, 0, 0, 0]. For comparison, note that Stolper et al. (2015) assume that the rate-limiting step, the only kinetic step, is step (7) in (13.15), which is mediated by *Mcr*, corresponding to [1, 1, 1, 1, 1, 1, 0]. This seems to be a common assumption.

The results of this exercise are summarized in Figure 13.4. The results for different assumptions about reversibility based on this reaction scheme show clearly that the very low Δ^{12}CH$_2$D$_2$ values and moderately low Δ^{13}CH$_3$D values of the gases produced by microbial methanogenesis are well explained by scenarios in which equilibrium for the first two or three steps in the reaction sequence in (13.16) obtains, with subsequent steps being kinetic. Indeed, Qi et al. (2014) suggested that step (3) in (13.16) is the likely rate-limiting step, with steps (1) and (2) being reversible. We note that the EIEs (defined as the reaction rate constant for hydrogen only divided by the rate constant for deuterium only) have typical values of order 0.6 compared with the KIEs defined similarly for the same reactions, which usually have values >1. The result is the production of extreme D/H ratios for the various pools of hydrogen atoms along the reaction sequence. For example, in the successful model [1, 1, 0, 0, 0, 0, 0], δD relative to the reactant hydrogen gas (0‰ in this case) is +125.6‰ for CH, 0.4‰ for CH$_2$, and −104.9‰ for CH$_3$ in this reaction scheme. Quantum tunneling of protium (H) and deuterium (D) may also play a role in the enzymatically catalyzed reactions, but we find that we can use a more conservative tunneling distance to fit the data than was used previously for the Sabatier reaction (see the caption to Figure 13.4). Notice that the results with all irreversible steps cannot explain the microbial methanogenesis data (Figure 13.4). Also, the [1, 1, 1, 1, 1, 1, 0] scheme in which the final step is rate limiting gives nonsensical results, with Δ^{12}CH$_2$D$_2$ and
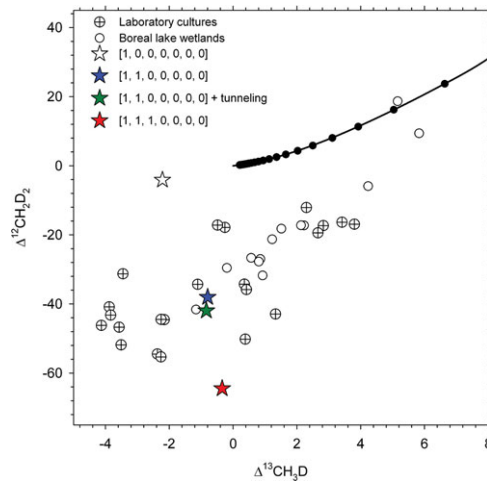
Figure 13.4 Summary of modeling reactions in (13.13) and (13.16). The stars represent model results for different combinations of equilibrium (signified by a 1 in the square brackets) or kinetic (signified by a 0 in the square brackets) steps during methane formation for the seven steps numbered in (13.16), as described in the text. Black dots denote equilibrium in $+50°C$ intervals starting with $0°C$ at the upper right. Circles show natural (open) and laboratory culture (crossed) data for microbial methanogenesis. The H tunneling distance used in the model that includes tunneling is 3×10^{-10} m with no carbon isotope effect. For the [1, 1, 0, 0, 0, 0] calculation, only steps (1) and (2) include isotopic equilibrium.

$\Delta^{13}CH_3D$ values of +138.4 and +11.3, showing that this scheme, analogous to that used by Stolper et al. (2015), is unlikely to be correct.

The reaction schemes resembling the microbial data in **Figure 13.4** also give realistic CH_4 δD and $\delta^{13}C$ bulk values for the product methane. For example, for the [1, 1, 0, 0, 0, 0, 0] scheme, we obtain CH_4 $\delta D = -161.2‰$ and $\delta^{13}C = -44.1‰$ relative to the hydrogen and carbon substrates.

Gruen et al. (2018) confirm that all four H atoms comprising CH_4 from hydrogenotrophic methanogenesis are from water, and yet we see profound disequilibrium in ΔCH_2D_2. While this simple model explains the first-order $\Delta^{12}CH_2D_2$ and $\Delta^{13}CH_3D$ characteristics of microbial methanogenesis, there is more to the kinetic story with respect to methane formation. Also, it should be pointed out that the highest $\Delta^{12}CH_2D_2$ and $\Delta^{13}CH_3D$ values near the equilibrium curve in **Figure 13.4** are boreal lake analyses that are evidently the result of methanotrophy (see below) rather than methanogenesis.

13.5 The Microbial Array

The positively sloping array in $\Delta^{12}CH_2D_2$ versus $\Delta^{13}CH_3D$ space defined by the *in vitro* and *in vivo* microbial methanogenesis data (**Figure 13.4**) cannot be explained easily by simply varying the degree of reversibility for the reaction steps. Quantum tunneling
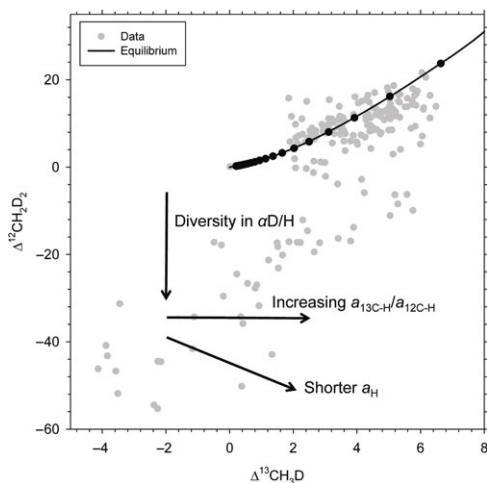
Figure 13.5 Vectors showing the effects of the key kinetic parameters controlling clumping during CH$_4$ formation.

involving both D/H and ^{13}C/^{12}C seems to be required. The involvement of carbon isotopes may at first seem unlikely. However, Miller et al. (1981) point out that it is incorrect to think of hydrogen tunneling in isolation. It is the reacting system as a whole that experiences tunneling, and if carbon atoms are involved in the reaction coordinate, the isotopic composition of the carbon can have an effect on tunneling. Using the same model reaction sequence described above, I have explored the interaction between various reversibility scenarios and the effects of tunneling. Generalized vectors showing the effects of the various parameters based on this exploration of parameter space are shown in Figure 13.5. Disparities in reversibility, and thus large differences in fractionation factors at each step, cause decreases in Δ^{12}CH$_2$D$_2$ at constant Δ^{13}CH$_3$D. This occurs with only moderately low δD for the product methane compared with the more extreme values caused by tunneling. Shorter hydrogen/deuterium tunneling distances increase the effects of quantum tunneling. Where the tunneling distance a_H is greater for reactions involving ^{13}C (as expected) than for ^{12}C, the slope of the enhancement in tunneling in Δ^{12}CH$_2$D$_2$ versus Δ^{13}CH$_3$D space is negative (Figure 13.5).

The effect of differences in tunneling distances involving ^{13}C versus ^{12}C can be visualized using a Marcus theory representation of tunneling shown in Figure 13.6; the lower energy of vibration for the ^{13}C–H bond relative to the C–H bond, for example, will necessitate a greater tunneling distance. The effect of $a_{13C–H}/a_{12C–H} > 1$ on Δ^{13}CH$_3$D can be understood as follows: the longer tunneling distance for the ^{13}C case gives less advantage to H relative to D in bonding with ^{13}C relative to the ^{12}C case, all else equal, and so ^{13}CH$_3$D is preferred relative to ^{13}CH$_4$. Thus, Δ^{13}CH$_3$D goes up.

The principles described in Figures 13.5 and 13.6 can be used to describe the "kinetic array" that lies well below the equilibrium curve in Figure 13.4. There is a hint that these
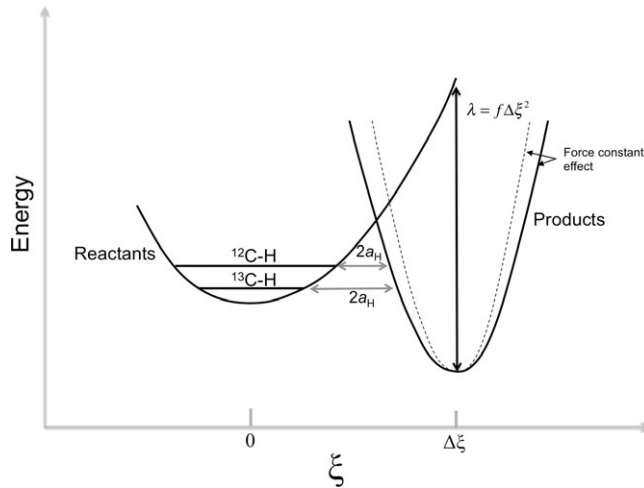
Figure 13.6 Schematic illustrating the relationship between carbon isotope substitution and tunneling. The ordinate is potential energy and the abscissa is the reaction coordinate ζ representing the interatomic motions leading to the reaction. The parabolas represent the potential energy of reactants and products in terms of interatomic distances along the reaction coordinate. The gray arrows shows the "tunneling" of hydrogen through the energy barrier associated with the transition from reactants to products. $2a_H$ is the tunneling distance for a hydrogen bonded to either ^{13}C or ^{12}C (see text). λ refers to the "reorganization" energy as defined in Marcus theory that depends on the force constant f and the separation between the two energy minima $\Delta\xi$.

principles may have applications beyond just microbial methanogenesis. The methane gases from the deeper levels of the Kidd Creek Mine study fall on the high $\Delta^{12}CH_2D_2$ and $\Delta^{13}CH_3D$ end of the microbial array (Young et al. 2017). These gases are confidently regarded as abiotic with no connection to microbial methanogenesis, as far as we know (Sherwood Lollar et al. 2007). Therefore, their continuity with the microbialgenic gases implies a fundamental kinetic link.

The high end of the kinetic array occupied by some of the microbial data and the Kidd Creek data can be explained by a larger role for both kinetics and tunneling. Removing the reversibility in all but step (1) and adjusting a_H and a_{13C-H}/a_{12C-H} to 5.2×10^{-11} m and 1.016, respectively, yields a fit to the Kidd Creek data and the high end of the microbial kinetic array (black star in Figure 13.7). The $^{13}C/^{12}C$ tunneling effect of 1.016 is squarely in the range found by Miller et al. (1981). The δD obtained in this model is −470.7‰ relative to the source of hydrogen, similar to the low values for the Kidd Creek methane.

Taken together, the two results for the two ends of the "kinetic array" based on the analogue model for methane formation suggest that the positively sloping array in $\Delta^{12}CH_2D_2$ versus $\Delta^{13}CH_3D$ space can be explained by a gradation from reversibility in some early key steps and a more limited role for tunneling on the lower end toward less reversibility and a larger role for tunneling on the higher end, including more participation of carbon in the reaction coordinate. In the case of the Kidd Creek data, it may make sense
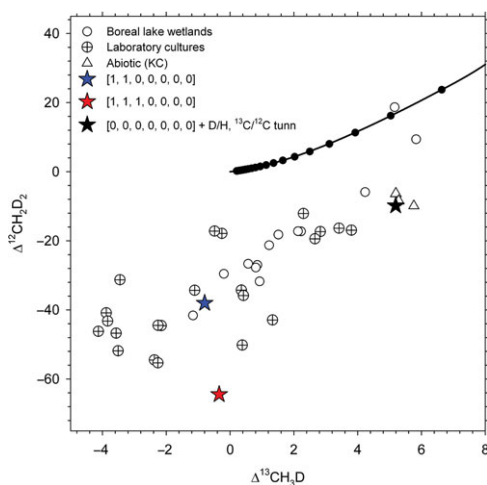
Figure 13.7 Comparison between the "kinetic array" in $\Delta^{12}CH_2D_2$ versus $\Delta^{13}CH_3D$ space and several relevant reaction rate models based on the reaction scheme shown in (13.13) and (13.16). The array may be defined by a "mixing" of the processes, similar to those depicted by the blue and black stars. See text for discussion. KC = Kidd Creek.

that catalysis of methane formation by metal surfaces would permit more of a role for carbon motions than in the case of the C_1 host molecules facilitating microbial methanogenesis.

13.6 Is This New Information Helping?

Is this new information about processes orthogonal to differences in isotopic reservoirs actually helping us determine the provenance of methane gases? We examine this question with the aid of Figure 13.8. Here, we plot ~170 natural CH_4 samples analyzed and vetted in our laboratory at UCLA to date as well as the culture experiments and several high-temperature Fischer–Tropsch experiments in $\Delta^{12}CH_2D_2$ versus $\Delta^{13}CH_3D$ space on the left and in the traditional Schoell plot (δD versus $\delta^{13}C$) on the right. Based on the clumping diagram, three groups of samples are selected as examples of "process end members" as a sort of test of the efficacy of considering process as a means of deducing provenance. Two of the three groups are easily defined and substantiated by laboratory experiments. The first of these are the natural samples that represent purely microbial methanogenesis based on their similarity to the combination of $\Delta^{12}CH_2D_2$ and $\Delta^{13}CH_3D$ values obtained in our *in vitro* culture experiments (in most cases these are from boreal wetlands). The second group comprises gases produced at high temperatures (meaning >100°C) that lie at or near to isotopologue thermodynamic equilibrium. While many of these gases are thermogenic, we are purposefully avoiding the traditional classification terminology at this stage because these terms can connote both process and the sources of carbon and hydrogen (e.g.
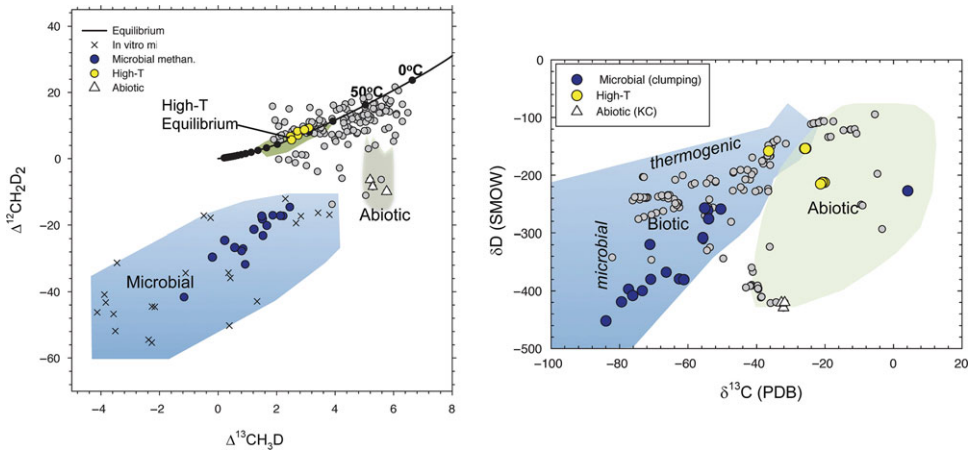
Figure 13.8 Comparison of data categorized by process in $\Delta^{12}CH_2D_2$ versus $\Delta^{13}CH_3D$ space (left panel) to their positions in the bulk isotope "Schoell" plot (right panel). Details are discussed in the text. Fields on the left are from the mass-18 isotopologue work, while the fields in bulk isotope space are from Etiope and Schoell (2014) and Etiope (2017). Gray symbols are data not categorized explicitly in this plot. The data labeled "microbial methane" are dominantly, although not entirely, from boreal lakes. PDB = Pee Dee Belemnite standard.

Sherwood Lollar et al. 2006; Etiope and Sherwood Lollar 2013). The third group represents "abiotic" methane. Here, we have immediately deviated from the strategy outlined in the previous sentence and introduced a measure of circularity into the classification by convolving it with source material. This is justified because of the overwhelming geological and geochemical evidence suggesting that the Kidd Creek Mine gases owe their origins to abiotic processes deep in the crust.

The three end-member processes are well separated on the left-hand panel of Figure 13.8. Those same data points, with the same color coding, are plotted on the Schoell plot on the right in Figure 13.8. I have added two major methane source fields, biotic and abiotic, as inspired by the fields shown in Etiope and Schoell (2014) and Etiope (2017). The microbial and thermogenic process subfields of the biotic field are also shown. Overall, the microbial gases as defined by the isotopic bond ordering plot in the microbial subfield for biotic gases in the Schoell plot. The high-temperature equilibrium gases tend to plot in the thermogenic subfield of the biotic field in the Schoell plot, and the Kidd Creek abiotic gases are at the lower edges of the abiotic field in the Schoell plot. Have we learned anything?

The answer appears to be yes because the isotopologue fields separate process from source material unambiguously. For example, the vertical (δD) positions of boreal wetland microbial methanogenesis data in the Schoell plot are lower than those for many "typical" microbial gases because the water δD values for these arctic environs are approximately $-200‰$ (e.g. Douglas et al. 2016 and references therein), rather lower than for waters from lower latitudes. The [1, 1, 0 . . . 0] kinetic model (blue star in Figure 13.7) predicts a

downward shift in δD of ~160‰ relative to the source hydrogen, yielding bulk δD values of about -360‰, consistent with the boreal wetland data in Figure 13.8. The breadth of the microbial field in the Schoell plot is therefore dictated in part by the range of source hydrogen and carbon samples independent of process. In isotopic bond ordering space, this effect is normalized out.

The importance of normalizing away reactant bulk isotopic compositions is best exemplified by the fact that there are instances where data falling squarely in the microbial field in $\Delta^{13}CH_3D$–$\Delta^{12}CH_2D_2$ space are not in the biotic field on the Schoell plot. The reasons for this can be traced to unexpected source materials (as enumerated in publications in preparation). Similarly, gases equilibrated at relatively high temperatures as evidenced in the $\Delta^{13}CH_3D$–$\Delta^{12}CH_2D_2$ plot span the biotic and abiotic fields in the Schoell plot.

Most of the other data points that appear in Figure 13.8 (undifferentiated data are shown in gray) that do not fall within one of the fields in $\Delta^{13}CH_3D$–$\Delta^{12}CH_2D_2$ space are the result of mixing, fractionation by molecular mass (e.g. Giunta et al. 2018), or possibly processes that are still under study (see Section 13.7).

As an illustrative example of both the high information content and the complexity afforded by CH_4 isotopologue data, we consider here a methane sample from a seafloor vent from the North Atlantic. It is generally thought that aqueous alteration of ultramafic rocks can produce abiotic methane as a by-product of serpentinization that releases hydrogen gas by a reaction resembling $3Fe_2SiO_4 + 2H_2O \rightarrow 2Fe_3O_4 + 3SiO_2 + 2H_2(g)$. However, the process is less clear than once thought due to severe kinetic limitations (McCollom 2016). The temperatures or kinetic pathways of methane formation in serpentinizing systems would be valuable arbiters for competing hypotheses for CH_4 formation in these settings. One well-studied site for methane production associated with active serpentinization is the Atlantis Massif that lies east of the intersection of the Mid-Atlantic Ridge and the Atlantis transform fault on the North Atlantic Ocean seafloor. The Lost City hydrothermal field from the southern Atlantis Massif has been of particular interest as the archetypical example of an off-axis seafloor hydrothermal alteration zone (Kelley et al. 2005). Fluids are venting at temperatures of ~30–90°C and both archaeal methanogens and methanotrophs are evidenced in the system (Kelley et al. 2005). Earlier studies indicated that serpentinization at the site was seawater dominated at temperatures of ~150–250°C (Allen and Seyfried Jr. 2004; Boschi et al. 2008). Proskurowski et al. (2006) used apparent D/H partitioning between CH_4, H_2, and H_2O to suggest that methane formation linked to serpentinization occurred at temperatures of ~110–150°C. Wang et al. (2018) used $\Delta^{13}CH_3D$ to estimate methane formation temperatures for several seafloor vent systems, including Lost City. Their $\Delta^{13}CH_3D$ value for the Beehive vent at Lost City is 1.84 ± 0.60‰ (95% confidence), from which they derive a methane formation temperature of 270 $+104/-68$°C. These authors discuss the evidence supporting this temperature, which is higher than many previous estimates.

At UCLA, we measured a methane sample from the Beehive vent at Lost City (collected in 2005 and provided by Marvin Lilly, University of Washington) and obtained $\Delta^{13}CH_3D = 1.95$‰ ± 0.40 (2σ) and $\Delta^{12}CH_2D_2 = 11.6$‰ ± 1.2 (2σ) (Figure 13.9). This
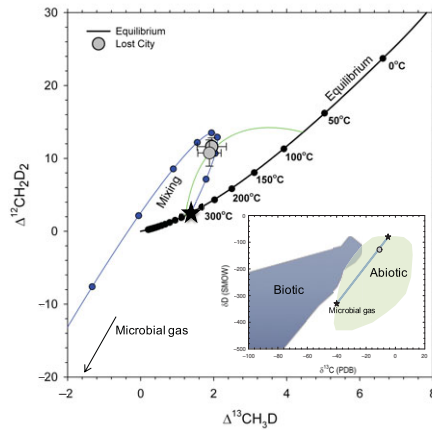
Figure 13.9 The mass-18 isotopologue data and bulk δ^{13}C and δD values for a sample from the Beehive vent of the Lost City hydrothermal field and two possible mixing scenarios to explain the data discussed in the text. Stars show end-member compositions for the missing scenario involving microbial gas described in the text. Solid dots on the mixing curve mark proportions in 10% increments. The Lost City data are the gray circles in both plots. Error bars are 2σ. PDB = Pee Dee Belemnite standard.

Δ^{13}CH$_3$D value is indistinguishable from the Wang et al. (2018) value, and thus at face value it is consistent with the high formation temperature (260 +58/–45°C in our case) obtained in the Wang et al. study. However, the Δ^{12}CH$_2$D$_2$ value is 7.5‰ higher than the equilibrium value at that temperature. Since the datum is displaced from the equilibrium curve (Figure 13.9), the Δ^{13}CH$_3$D value of 1.95 cannot be taken *a priori* as a direct measure of methane bond formation temperature.

The position of the Lost City sample above the equilibrium curve in Figure 13.9 suggests that the gas is a mixture. One mixture that fits the datum within error is composed of 20% microbial gas and 80% high-temperature (~350°C) abiotic gas (blue curve in Figure 13.9). The bulk isotopic compositions of these two end members and the associated mixing curve in bulk isotope ratio space are shown in the inset in Figure 13.9. The end-member δ^{13}C and δD values required by the fit to the Δ^{13}CH$_3$D and Δ^{12}CH$_2$D$_2$ data are reasonable, if imperfect, representatives of microbial methanogenesis and abiotic gas, respectively. In this case, the methane isotopologue data may be indicative of a microbial methanogenesis component to the Lost City gas, whereas any temperature information for the mixture end members is model dependent. While the mixing scenario described above is plausible, the Lost City datum by itself does not lead to an entirely unique interpretation. For example, a fit to the isotopologue data can also be obtained by mixing 375°C and 75°C gases with abiotic-like δ^{13}C and δD values of −20 and −60‰ and −3.5 and −183‰, respectively (green curve in Figure 13.9).

Possible explanations for the Lost City data other than mixing are: (1) the bulk isotopic composition of the gas was altered by a process that fractionates isotopologues by molecular mass, moving the gas along a slope-1 line in Figure 13.9 and thus suggesting a low formation temperature of ~75°C by extrapolation back to the equilibrium curve; or (2) combinations of mixing and fractionation.

The Lost City example shows at once the potential power of the methane isotopologue data, but also the complexity in the interpretations that can arise, especially where the data are sparse. Of course, suites of data representing ranges in composition are more diagnostic than individual data points. Among the data shown in Figure 13.8 are examples of linear trends in $\Delta^{12}CH_2D_2$ versus $\Delta^{13}CH_3D$ space with slopes of unity that are telltale signs of fractionation by molecular mass, for example.

The ability to use rare isotopologue abundances rather than bulk isotope ratios as means of tracing the origins of methane gases could have important applications elsewhere in the solar system. Measuring $\Delta^{12}CH_2D_2$ and $\Delta^{13}CH_3D$ in methane from the atmospheres of Mars or Saturn's moon Titan, for example, would provide powerful evidence for the formation mechanisms of Martian and Titanian methane even where the meaning of bulk $^{13}C/^{12}C$ and D/H in the methane is hampered by unknown chemical cycles on those bodies.

13.7 The Effects of Oxidation on $\Delta^{12}CH_2D_2$ and $\Delta^{13}CH_3D$

It appears that the combination of values for $\Delta^{12}CH_2D_2$ and $\Delta^{13}CH_3D$ provides a signature of microbialgenic methane (the microbial array) that is independent of bulk isotope ratios, and therefore independent of sources of carbon and hydrogen. The uniqueness of the low $\Delta^{13}CH_3D$ and extremely low $\Delta^{12}CH_2D_2$ values that in combination signify microbial methanogenesis depends on whether other processes might mimic this effect. We have *in vitro* evidence that anaerobic oxidation of methane (AOM) tends to drive isotopologue compositions of methane toward equilibrium and away from the microbial array. However, at time of writing, the effects of bacterial aerobic oxidation of methane remain unknown.

The data clustered near the equilibrium curve in the upper right of the $\Delta^{12}CH_2D_2$ versus $\Delta^{13}CH_3D$ diagram (e.g. left panel of Figure 13.8) present a vexing problem. At face value, these gases are in near isotopologue equilibrium at <50°C. Two prominent examples are a few of the boreal wetland samples and some of the deep mine samples. However, it seems unlikely that CH$_4$ gas would equilibrate at such low temperatures absent a reaction that breaks and reforms methane molecules (as opposed to isotope exchange with water, for example, which is slow; e.g. Sessions et al. 2004). What is this process?

Young et al. (2017) postulated that the evolution of CH$_4$ effusing from the Kidd Creek Mine fluids over several years from the disequilibrium abiotic field toward the equilibrium curve is the result of cycling between microbial methanogenesis and methanotrophy. The shifts over time are seen mainly in $\Delta^{12}CH_2D_2$, which is initially in gross disequilibrium, but not in $\Delta^{13}CH_3D$, where the latter is in apparent equilibrium from the start (Figure 13.3).

This cycling may or may not be distinct from the "cryptic methane cycle" described recently by Maltby et al. (2018) and Xiao et al. (2017); the cryptic methane cycle refers to high SO_4 noncompetitive environs, while experiments suggest that methane reemitted by AOM is driven by low concentrations of the electron acceptor (e.g. SO_4; see below). In addition, based on samples from Baltic Sea sediments, Ash et al. (2019) find evidence that isotopic bond-order equilibrium in these sediments is the result of AOM. Stolper et al. (2015) had hypothesized that AOM might yield thermodynamic equilibrium among methane isotopologues, suggesting that isotopic equilibrium between CH_4, H_2, and CO_2 would ensue. The Baltic Sea results suggest that CH_4 equilibration occurs without equilibrium with water. The concept that AOM has the capacity to yield methane in isotopic bond-order equilibrium builds on the earlier work of Holler et al. (2011) and Yoshinaga et al. (2014) showing that AOM can lead to $^{13}C/^{12}C$ equilibrium. AOM shares enzymatic machinery with microbial methanogenesis, leading to the notion that AOM is a reversal of methanogenesis (Scheller et al. 2010; Timmers et al. 2017). Indeed, Yan et al. (2018) report Fe-based AOM by the methanogen *Methanosarcina acetivorans* in which oxidation of methane occurs by the reversal of the biochemical pathway for acetoclastic and CO_2 reduction to methane (see (13.17)). The influence of AOM on the isotopologue composition of CH_4 in nature seems plausible; Yoshinaga et al. (2014) point out that methanogens represent a small contingent of the microbial communities in AOM-active sediments and that $^{14}CO_2$ is converted to $^{14}CH_4$ in sulfate–methane transition zones (Orcutt et al. 2005).

Confounding the identification of the CH_4 isotopologue signature of AOM in natural settings is the contradictory evidence for its bulk isotopic effects. While Holler et al. (2009) found increases in bulk $^{13}C/^{12}C$ and D/H in residual methane left behind by AOM in the laboratory, Yoshinaga et al. (2014) emphasized that methane from sulfate-limited AOM horizons has a relatively low $\delta^{13}C$ value, not high as expected from simple classical kinetics. They suggest that this is due to equilibration of $^{13}C/^{12}C$ in the back reaction to convert dissolved inorganic carbon (CO_2 dissolved in water) to CH_4.

Douglas et al. (2017) refer to "differential reversibility of methanogenesis" in the context of explaining various degrees of apparent equilibration of $\Delta^{13}CH_3D$ (or Δ_{18}) values for methane. They suggest that hydrogenotrophic, H_2-limited methanogenesis (Valentine 2011) causes reversibility. They attribute the equilibrium to rapid H/D exchange with water. This interpretation is in the context of the "reversibility of methanogensis" hypothesis rather than reversibility in AOM. These earlier suggestions notwithstanding, the $\Delta^{12}CH_2D_2$ versus $\Delta^{13}CH_3D$ data suggest that interspecies (e.g. CH_4 versus H_2O) equilibration is not a requisite for intraspecies (CH_4 alone) equilibration.

Because of the difficulty in equilibrating isotopologues at low (near room) temperatures and because of the circumstantial evidence for AOM in several of the sites where low-temperature equilibration in methane gas is evidenced in the isotopologue data, experiments are underway attempting to characterize the $\Delta^{12}CH_2D_2$ versus $\Delta^{13}CH_3D$ effects of AOM. These include experiments by J. Gregory Ferry's group at Penn State University that comprise exchange of the methyl moiety in methyl-coenzyme M (CH_3-SCOM) and CH_4 by the reaction couple
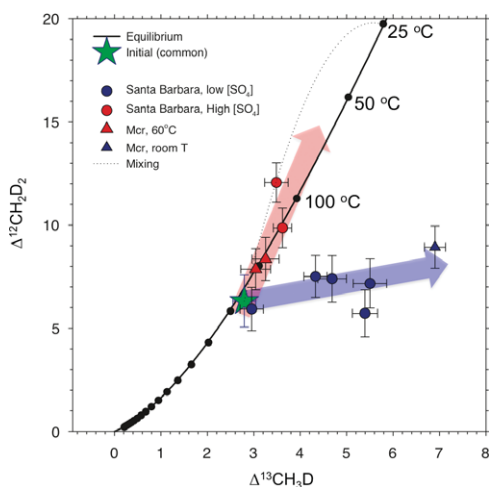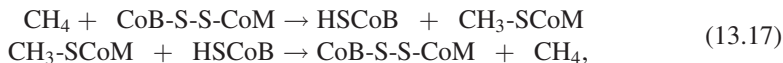
Figure 13.10 Summary of preliminary AOM *in vitro* experiments in $\Delta^{12}CH_2D_2$ versus $\Delta^{13}CH_3D$ space. Symbol shapes distinguish the two sets of experiments. The star shows the initial gas composition of the Santa Barbara slurry experiments. The *Mcr* experiments are migrated so that they are relative to the Santa Barbara initial gas composition. The arrows shows the two different trends that are evident in the data as described in the text. Equilibrium temperatures strictly apply only to the Santa Barbara experiments due to the migration of the *Mcr* data.

$$
\begin{aligned}
CH_4 + \ CoB\text{-}S\text{-}S\text{-}CoM &\rightarrow HSCoB \ + \ CH_3\text{-}SCoM \\
CH_3\text{-}SCoM \ + \ HSCoB &\rightarrow CoB\text{-}S\text{-}S\text{-}CoM \ + \ CH_4,
\end{aligned}
\tag{13.17}
$$

where HSCoB is coenzyme B that provides the proton and CoB-S-S-CoM is the hetero-disulfide of coenzymes M and B that serves as the oxidant in the reaction. Reaction (13.17) is catalyzed by the *Mcr* enzyme and is a reversible instance of the final step in (13.15). This experiment is particularly informative as it isolates the step that is often cited as the source of equilibration. The hypothesis is that the reversibility of this step might capture the mechanism for CH$_4$ isotopologue equilibration by AOM. Accordingly, the expectation was that we would see reactant methane in the headspace for this cocktail of coenzymes progress toward isotopologue equilibration.

Some preliminary results from the Penn State experiments are shown in Figure 13.10. The data define two trends. At temperatures below those optimal for the *Mcr* used in the experiments (near room temperature), there is a trend toward equilibrium values for $\Delta^{13}CH_3D$ but little change in $\Delta^{12}CH_2D_2$. At 60°C, the optimal temperature for the thermophile-derived enzyme, there are modest but discernible increases in both $\Delta^{13}CH_3D$ and $\Delta^{12}CH_2D_2$ values (Figure 13.10). The higher-temperature experiments presumably involve greater turnover of methane by enzymatic activity and thus more exchange of hydrogen. Based on the modeling summarized in Figure 13.4, the positive shift in $\Delta^{13}CH_3D$ at relatively constant $\Delta^{12}CH_2D_2$ observed in the low-temperature

experiments suggests that carbon played a larger role than hydrogen in affecting the isotopologue abundances resulting from exchange.

In a set of parallel experiments by Tina Treude's laboratory at UCLA, methane headspace gas was consumed by SO_4-limited AOM in *in vitro* marine sediment slurries using samples collected from active methane seeps in the Santa Barbara channel off the coast of Santa Barbara, California. Methane incubations lasted for various time intervals in the order of days to weeks with concentrations of SO_4 ranging from 38 mM to $<$500 μM. The low-SO_4 incubations resemble the low-temperature *Mcr* experiments in which the $\Delta^{13}CH_3D$ values of residual headspace methane increased toward equilibrium while $\Delta^{12}CH_2D_2$ remained relatively constant. However, the higher concentration of SO_4 results resemble the higher-temperature *Mcr* experiments, with both $\Delta^{12}CH_2D_2$ and $\Delta^{13}CH_3D$ increasing with methane consumption (Figure 13.10). One datum from the Santa Barbara sediment slurry experiments lies above the equilibrium curve and might be explained by mixing between initial gas and equilibrated gas, as shown by the dotted curve in Figure 13.10.

These experiments are ongoing, and more detailed reports are in preparation, but our preliminary conclusion is that AOM can push residual methane toward $\Delta^{12}CH_2D_2$ and $\Delta^{13}CH_3D$ equilibrium on trajectories in $\Delta^{12}CH_2D_2$ and $\Delta^{13}CH_3D$ space that depend on the conditions. Where the enzymatically facilitated exchange is active, both $\Delta^{12}CH_2D_2$ and $\Delta^{13}CH_3D$ are affected, while under more restricted exchange activity, only $\Delta^{13}CH_3D$ is affected. Under no conditions do the effects of AOM resemble those for microbial methanogenesis in $\Delta^{12}CH_2D_2$ and $\Delta^{13}CH_3D$ space.

Aerobic microbial oxidation effects on $\Delta^{13}CH_3D$ were studied by Wang et al. (2016), in which $\Delta^{13}CH_3D$ values were observed to decrease by several per mil with methane consumption. The effects on $\Delta^{12}CH_2D_2$ are as yet not known from experiments. Oxidation of methane in the atmosphere by Cl or OH radicals was investigated experimentally by Whitehill et al. (2017) for $^{12}CH_4$, $^{13}CH_4$, $^{12}CH_3D$, and $^{13}CH_3D$ (i.e. $\Delta^{13}CH_3D$). The effects of Cl and OH oxidation of methane on $^{12}CH_2D_2$ (i.e. $\Delta^{12}CH_2D_2$) as well as on the other species was modeled by Haghnegahdar et al. (2017). The predictions for $\Delta^{12}CH_2D_2$ effects of Cl and OH oxidation have been verified by measurements of the experimental products produced by Whitehill et al. (2017) at UCLA. All of these results on the Cl and OH oxidation of methane indicate large shifts in clumping down to extremely low $\Delta^{12}CH_2D_2$ values (negative tens of per mil) and low $\Delta^{13}CH_3D$ values well below zero. What is more, in each of the studies, the isotopic KIE values (kinetic isotope fractionation factors) associated with the simple reactions $CH_4 + OH \rightarrow CH_3 + H_2O$ and $CH_4 + Cl \rightarrow CH_3 + HCl$ closely approximate the "rule of the geometric mean" (RGM) (Bigeleisen 1955) in which the KIE for $^{13}CH_3D/CH^4$, for example, is the product of those for $^{13}CH_4/CH_4$ and $^{12}CH_3D/CH_4$, etc. Where the RGM applies, the relative abundances of the multiply substituted isotopologues – $^{13}CH_3D$ and $^{12}CH_2D_2$ in this application – are controlled entirely by the classical KIEs and not by the equilibrium zero-point energy effects specific to each of the isotopologues. The results of the classical kinetics in which the lighter isotopic species of methane react with Cl and OH more rapidly than the heavier

isotopologues are increases in bulk ^{13}C/^{12}C and D/H in the residual methane left behind and concomitant decreases in Δ^{12}CH$_2$D$_2$ and Δ^{13}CH$_3$D (see Question 1 in the "Questions for the Classroom" section for the proof of this behavior). One expects the RGM to apply for single-step kinetic reactions such as those that oxidize CH$_4$ in the atmosphere. The RGM does not apply to the methane isotopologue effects of AOM. Whether the RGM applies to aerobic bacterial oxidation is at present not known, but experiments are planned.

13.8 Conclusions

Isotopic bond ordering in methane gas molecules traces process, while bulk isotope ratios trace both process and source isotopic compositions. By measuring the isotopic bond ordering in CH$_4$ gas, it is possible to isolate processes from sources. The ^{13}C/^{12}C ratios of microbialgenic methane, for example, are controlled by the substrate carbon as well as by the processes of methane formation. The D/H ratios of methane are controlled by the source of hydrogen (often water), as well as the reaction path to formation. The combination of Δ^{13}CH$_3$D and Δ^{12}CH$_2$D$_2$ yields a measure of the process of formation irrespective of the ^{13}C/^{12}C or the D/H ratios of the source carbon and hydrogen. While more experimental work is required to investigate all possible reaction pathways, thus far it appears that the position of a methane datum in Δ^{13}CH$_3$D versus Δ^{12}CH$_2$D$_2$ space can be used to identify processes of formation independent of the uncertainties in the source material. One can predict that the ability to trace the origins of methane independent of bulk carbon and hydrogen isotope ratios could prove invaluable for assessing the origins of CH$_4$ gas on other solar system bodies where the meaning of bulk isotope ratios would not be accurately known.

13.9 Limits to Knowledge and Unknowns

A known unknown is the effect of "cracking" of organics in Δ^{13}CH$_3$D versus Δ^{12}CH$_2$D$_2$ space. Thus far, it seems that low – even negative – values for Δ^{12}CH$_2$D$_2$ result from the multiple steps of building a CH$_4$ molecule as in microbial methanogenesis. For comparison, Shuai et al. (2018) found that while nonhydrous pyrolysis of coal can generate methane with equilibrium Δ^{13}CH$_3$D (Δ_{18}) values at temperatures ranging from ~400°C to ~500°C and from ~600°C to 700°C, disequilibrium in Δ_{18} by about 2‰ results from ~500°C to ~600°C. The degree of disequilibrium also depends on the rate of heating. Based on these results, an important question is whether such processes could ever lead to confusion between microbial methanogenesis and cracking in Δ^{13}CH$_3$D versus Δ^{12}CH$_2$D$_2$ space. Hydrous pyrolysis of shale evidently leads to equilibrium isotopologue distributions in the product methane (Shuai et al. 2018). It is perhaps relevant in this context that the temperature window leading to disequilibrium in methane isotopologues due to pyrolysis seems to be rather narrow, suggesting that this may not be a generally important process. More experiments are required.

Acknowledgments

Questions for the Classroom

1 Why would partial consumption of isotopically light methane molecules leave the residual methane with lower $\Delta^{13}CH_3D$ and $\Delta^{12}CH_2D_2$ values relative to the initial isotopologue composition of the gas in the absence of isotopic exchange among the methane molecules?

2 Why do lower temperatures favor greater $\Delta^{13}CH_3D$ and $\Delta^{12}CH_2D_2$ values relative to the stochastic values of zero?

3 Why are $\Delta^{13}CH_3D$ and $\Delta^{12}CH_2D_2$ values independent of bulk isotope ratios?

References

Allen D. E. and Seyfried Jr. W. E. (2004) Serpentinization and heat generation: constraints from Lost City and Rainbow hydrothermal systems. *Geochemica et Cosmochimica Acta* **68**(6): 1347–1354.

Ash J. L., Egger M., Treude T., Kohl I., Cragg B., Parkes R., Slomp C., Sherwood Lollar B. and Young E. D. (2019) Exchange catalysis during anaerobic methanotrophy revealed by $^{12}CH_2D_2$ and $^{13}CH_3D$ in methane. *Geochemical Perspectives Letters* **10**: 26–30.

Bell R. P. (1959) The tunnel effect correction for parabolic potential barriers. *Transactions of the Faraday Society* **55**: 1–4.

Bell R. P. (1980) *The Tunnel Effect in Chemistry*. London, Chapman & Hall.

Bigeleisen J. (1955) Statistical mechanics of isotopic systems with small quantum corrections. I. General considerations and the rule of the geometric mean. *Journal of Chemical Physics* **23**(12): 2264–2267.

Boschi C., Dini A., Fruh-Green G. L. and Kelley D. S. (2008) Isotopic and element exchange during serpentinization and metasomatism at the Atlantis Massif (MAR 30°N): insights from B and Sr isotope data. *Geochemica et Cosmochimica Acta* **72**: 1801–1823.

Cao X., Bao H. and Peng Y. (2019) A kinetic model for isotopologue signatures of methane generated by biotic and abiotic CO_2 methanation. *Geochimica et Cosmochimica Acta* **249**: 59–75.

Douglas P. M., Stolper D. A., Eiler J. M., Sessions A. L., Lawson M., Shuai Y., Bishop A., Podlaha O. G., Ferreira A. A., Neto E. V. S., Niemann M., Steen A. S., Huang L., Chimiak L., Valentine D. L., Fiebig J., Luhmann A. J., Seyfried W. E. J., Etiope G., Schoell M., Inskeep W. P., Moran J. J. and Kitchen N. (2017) Methane clumped isotopes: progress and potential for a new isotopic tracer. *Organic Geochemistry* **113**: 262–282.

Douglas P. M. J., Stolper D. A., Smith D. A., Anthony K. M. W., Paull C. K., Dallimore S., Wik M., Crill P. M., Winterdahl M., Eiler J. M. and Sessions A. L. (2016) Diverse origins of Arctic and subarctic methane point source emissions identified with multiply-substituted isotopologues. *Geochemica et Cosmochimica Acta* **188**: 163–188.

Eiler J. M., Ghosh P., Affek H., Schauble E., Adkins J., Schrag D. and Hoffman P. (2005). Carbonate plaeothermometry based on abundances of 13C–18O bonds. Presented at: *Goldschmidt Conference*, Moscow, Idaho, A127l.

Etiope G. (2017) Methane origin in the Samail ophiolite: comment on "Modern water/rock reactions in Oman hyperalkaline peridotite aquifers and implications for microbial habitability" [*Geochem. Cosmochim. Acta* 179 (2016) 217–24]. *Geochemica et Cosmochimica Acta* **197**: 467–470.

Etiope G. and Schoell M. (2014) Abiotic gas: atypical, but not rare. *Elements* **10**: 291–296.

Etiope G. and Sherwood Lollar B. (2013) Abiotic methane on Earth. *Reviews of Geophysics* **51**: 276–299.

Giunta T., Young E. D., Warr O., Kohl I., Ash J. L., Martini A. M., Mundle S. A. C., Rumble D., Perez-Rodriquez I., Wasley M., LaRowe D. E., Gilbert A. and Sherwood Lollar B. (2018) Methane sources and sinks in continental sedimentary basins: new insights from paired clumped isotopologues $^{13}CH_3D$ and $^{12}CH_2D_2$. *Geochemica et Cosmochimica Acta* **245**: 327–351 (2019).

Gruen D. S., Wang D. T., Konneke M., Topcuoglu B. D., Stewart L. C., Goldhammer T., Holden J. F., Hinrichs K.-U. and Ono S. (2018) Experimental investigation on the controls of clumped isotopologue and hydrogen isotope ratios in microbial methane. *Geochemica et Cosmochimica Acta* **237**: 339–356.

Haghnegahdar M., Schauble E. A. and Young E. D. (2015) Constructing an atmospheric methane budget using $^{13}CH_3D$ and CH_2D_2 in sources and sinks. Presented at: *American Geophysical Union*, 82743l.

Haghnegahdar M. A., Schauble E. and Young E. D. (2017) A model for $^{12}CH_2D_2$ and $^{13}CH_3D$ as complementary tracers for the budget of atmospheric CH_4. *Global Biogeochemical Cycles* **31**: 1387–1407.

Holler T., Wegener G., Knittel K., Boetius A., Brunner B., Kuypers M. M. and Widdel F. (2009) Substantial $^{13}C/^{12}C$ and D/H fractionation during anaerobic oxidation of methane by marine consortia enriched *in vitro*. *Environmental Microbiology Reports* **1**: 370–376.

Holler T., Wegener G., Niemann H., Deusner C., Ferdelman T. G., Boetius A., Brunner B. and Widdel F. (2011) Carbon and sulfur back flux during anaerobic microbial oxidation of methane and coupled sulfate reduction. *Proceedings of the National Academy of Sciences* **108**: E1484–E1490.

Kelley D. S., Karson J. A., Fruh-Green G. L., Yoerger D. R., Shank T. M., Butterfield D. A., Hayes J. M., Shrenk M. O., Olson E. J., Proskurowski G., Jakuba M., Bradley A., Larson B., Ludwig K., Glickson D., Buckman K., Bradley A. S., Brazelton W. J., Roe K., Elend M. J., Delacour A., Bernasconi S. M., Lilley M. D., Baross J. A., Summons R. E. and Sylva S. P. (2005) A serpentinite-hosted ecosystem: the Lost City hydrothermal field. *Science* **307**: 1428–1434.

Lieber D. J., Catlett J., Madayiputhiya N., Nandakumar R., Lopez M. M., Metcalf W. M. and Buan N. R. (2014) A multienzyme complex channels substrates and electrons through acetyl-CoA and methane biosynthesis pathways in Methanosarcina. *PLoS ONE* **9**(9): e107563.

Liu Q. and Liu Y. (2016) Clumped-isotope signatures at equilibrium of CH_4, NH_3, H_2O, H_2S and SO_2. *Geochemica et Cosmochimica Acta* **175**: 252–270.

Ma Q., Wu S. and Tang Y. (2008) Formation and abundance of doubly-substituted methane isotopologues ($^{13}CH_3D$) in natural gas systems. *Geochemica et Cosmochimica Acta* **72**(22): 5446–5456.

Maltby J., Steinle L., Loscher C. R., Bange H. W., Fischer M. A., Schmidt M. and Treude T. (2018) Microbial methanogensis in the sulfate-reducing zone of sediments in the Eckernforde Bay, W Baltic Sea. *Biogeosciences* **15**: 137–157.

McCollom T. M. (2016) Abiotic methane formation during experimental serpentinization of olivine. *Proceedings of the National Academy of Sciences* **113**: 13965–13970.

Miller D. J., Subramanian R. and Saunders W. H. J. (1981) Mechanisms of elimination reactions. 33. Carbon isotope effects in E2 reactions of (2-phenylethyl-2-^{14}C)trimehylammonium ion. The role of tunneling. *Journal of the American Chemical Society* **103**: 3519–3522.

Orcutt B., Boetius A., Elbert M., Samarkin V. and Joye S. B. (2005) Molecular biogeochemistry of sulfate reduction, methanogenesis and anaerobic oxidation of methane at Gulf of Mexico cold seeps. *Geochemica et Cosmochimica Acta* **69**: 4267–4281.

Penning H., Plugge C. M., Galand P. E. and Conrad R. (2005) Variation of carbon isotope fractionation in hydrogenotrophic methanogenic microbial cultures and environmental samples at different energy status. *Global Change Biology* **11**(12): 2103–2113.

Proskurowski G., Lilley M. D., Kelley D. S. and Olson E. J. (2006) Low temperature volatile production at the Lost City hydrothermal field, evidence from a hydrogen stable isotope geothermometer. *Chemical Geology* **229**: 331–343.

Qi Y., Yang J., Duan X., Zhu Y.-A., Chen D. and Holmen A. (2014) Discrimination of the mechanism of CH_4 formation in Fischer–Tropsch synthesis on Co catalysts: a combined approach of DFT, kinetic isotope effects and kinetic analysis. *Catalysis Science & Technology* **4**: 3534–3542.

Richet P., Bottinga Y. and Javoy M. (1977) A review of hydrogen, carbon, nitrogen, oxygen, sulphur, and chlorine stable isotope fractionation among gaseous molecules. *Annual Reviews in Earth and Planetary Science* **5**: 65–110.

Rockmann T., Popa M. E., Krol M. C. and Hofmann M. E. G. (2016) Statistical clumped isotope signatures. *Scientific Reports* **6**: 31947.

Scheller S., Goenrich M., Boecher R., Thauer R. K. and Juan B. (2010) The key nickel enzyme of methanogenesis catalyses the anaerobic oxidation of methane. *Nature* **465**: 606–609.

Schoell M. (1980) The hydrogen and carbon isotopic composition of methane from natural gases of various origins. *Geochemica et Cosmochimica Acta* **44**: 649–661.

Sessions A. L., Sylva S. P., Summons R. E. and Hayes J. M. (2004) Isotopic exchange of carbon-bound hydrogen over geologic timescales. *Geochimica et Cosmochimica Acta* **68**: 1545–1559.

Sherwood Lollar B., Lacrampe-Couloume G., Slater G. F., Ward J., Moser D. P., Gihring T. M., Lin L.-H. and Onstott T. C. (2006) Unravelling abiogenic and biogenic sources of methane in the Earth's deep subsurface. *Chemical Geology* **226**: 328–339.

Sherwood Lollar B., Voglesonger K., Lin L.-H., Lacrampe-Couloume G., Telling J., Abrajano T. A., Onstott T. C. and Pratt L. M. (2007) Hydrogeologic controls on episodic H₂ release from Precambrian fractured rocks – energy for deep subsurface life on Earth and Mars. *Astrobiology* **7**(6): 971–986.

Shima S., Warkentin E., Thauer R. K. and Ermler U. (2002) Structure and function of enzymes involved in the methanogenic pathway utilizing carbon dioxide and molecular hydrogen. *Journal of Bioscience and Bioengineering* **93**: 519–530.

Shuai Y., Douglas P. M. J., Zhang S., Stolper D. A., Ellis G. S., Lawson M., Lewan M., Formolo M., Jingkui M., He K., Hu G. and Eile J. M. (2018) Equilibrium and non-equilibrium controls on the abundances of clumped isotopologues of methane during thermogenic formation in laboratory experiments: implications for the chemistry of pyrolysis and the origins of natural gases. *Geochimica et Cosmochimica Acta* **223**: 159–174.

Stolper D. A., Lawson M., Davis C. L., Ferreira A. A., Santos Neto E. V., Ellis G. S., Lewan M. D., Martini A. M., Tang Y., Schoell M., Sessions A. L. and Eiler J. M. (2014) Formation temperatures of thermogenic and biogenic methane. *Science* **344**: 1500–1503.

Stolper D. A., Martini A. M., Clog M., Douglas P. M., Shusta S. S., Valentine D. L., Sessions A. L. and Eiler J. M. (2015) Distinguishing and understanding thermogenic and biogenic sources of methane using multiply substituted isotopologues. *Geochemica et Cosmochimica Acta* **161**: 219–247.

Timmers P. H. A., Welte C. U., Koehorst J. J., Plugge C. M., Jetten M. S. M. and Stams A. J. M. (2017) Reverse methanogenesis and respiration in methanotrophic archaea. *Archaea* **2017**: 1654237.

Valentine D. L. (2011) Emerging topics in marine methane biogeochemistry. *Annual Review of Marine Science* **3**: 147–171.

Valentine D. L., Chidthaisong A., Rice A., Reeburgh W. S. and Tyler S. C. (2004) Carbon and hydrogen isotope fractionation by moderately thermophilic methanogens. *Geochemica et Cosmochimica Acta* **68**: 1571–1590.

Wang D. T., Gruen D. S., Sherwood Lollar B., Hinrichs K.-U., Stewart L. C., Holden J. F., Hristov A. N., Pohlman J. W., Morrill P. L., Könneke M., Delwiche K. B., Reeves E. P., Sutcliffe C. N., Ritter D. J., Seewald J. S., McIntosh J. C., Hemond H. F., Kubo M. D., Cardace D., Hoehler T. M. and Ono S. (2015) Nonequilibrium clumped isotope signals in microbial methane. *Science* **348**: 428–431.

Wang D. T., Reeves E. P., McDermott J. M., Seewald J. S. and Ono S. (2018) Clumped isotopologue constraints on the origin of methane at seafloor hotsprings. *Geochemica et Cosmochimica Acta* **223**: 141–158.

Wang D. T., Welander P. V. and Ono S. (2016) Fractionation of the methane isotopologues $^{13}CH_4$, $^{12}CH_3D$, and $^{13}CH_3D$ during aerobic oxidation of methane by Methylococcus capsulatus (Bath). *Geochemica et Cosmochimica Acta* **192**: 186–202.

Wang W., Wang S., Ma X. and Gong J. (2011) Recent advances in catalytic hydrogenation of carbon dioxide. *Chemical Society Reviews* **40**: 3703–3727.

Webb M. A. and Miller T. F., III (2014) Position-specific and clumped stable isotope studies: comparison of the Urey and path-integral approaches for carbon dioxide, methane, and propane. *Journal of Physical Chemistry* **118**: 467–474.

Whitehill A. R., Joelsson L. M. T., Schmidt J. A., Wang D. T., Johnson M. W. and Ono S. (2017) Clumped isotope effects during OH and Cl oxidation of methane. *Geochemica et Cosmochimica Acta* **196**: 307–325.

Xiao K.-Q., Beulig F., Kjeldsen K. U., Jorgensen B. B. and Risgaard-Petersen N. (2017) Concurrent methane production and oxidation in surface sediment from Aarhus Bay, Denmark. *Frontiers in Microbiology* **8**: 1198.

Yan Z., Joshi P., Gorski C. A. and Ferry J. G. (2018) A biochemical framework for anaerobic oxidation of methane driven by Fe(III)-dependent respiration. *Nature Communications* **9**: 1642.

Yeung L. Y. (2016) Combinatorial effects on clumped isotopes and their significance in biogeochemistry. *Geochemica et Cosmochimica Acta* **172**: 22–38.

Yeung L. Y., Ash J. L. and Young E. D. (2015) Biological signatures in clumped isotopes of O_2. *Science* **348**(6233): 431–434.

Yoshinaga M. Y., Holler T., Goldhammer T., Wegener G., Pohlman J. W., Brunner B., Kuypers M. M. M., Hinrichs K.-U. and Elvert M. (2014) Carbon isotope equilibration during sulphate-limited anaerobic oxidation of methane. *Nature Geoscience* **7**: 190–194.

Young E. D., Kohl I. D., Sherwood Lollar B., Etiope G., Rumble III D., Li S., Haghnegahdar M., Schauble E. A., McCain K. A., Foustoukos D. I., Sutcliffe C. N., Warr O., Ballentine C. J., Onstott T. C., Hosgormez H., Neubeck A., Marques J. M., Perez-Rodriquez I., Rowe A. R., LaRowe D. E., Magnabosco C., Yeung L. Y., Ash J. L. and Bryndzia L. T. (2017) The relative abundances of resolved $^{12}CH_2D_2$ and $^{13}CH_3D$ and mechanisms controlling isotopic bond ordering in abiotic and biotic methane gases. *Geochemica et Cosmochimica Acta* **203**: 235–264.

Young E. D., Rumble III D., Freedman P. and Mills M. (2016) A large-radius high-mass-resolution multiple-collector isotope ratio mass spectrometer for analysis of rare isotopologues of O_2, N_2, CH_4 and other gases. *International Journal of Mass Spectrometry* **401**: 1–10.